Comparison of 2D and 3D region-based deformable models and random walker methods for PET segmentation

Kévin Gosse, Stéphanie Jehan-Besson, François Lecellier, Su Ruan

Comparison of 2D and 3D Region-based Deformable Models and Random Walker Methods for PET Segmentation

Kévin Gosse[1], Stéphanie Jehan-Besson[1], François Lecellier[2], Su Ruan[3]
[1] Groupe de recherche en Informatique, Image, Automatique et Instrumentation de Caen
Normandie Univ, UNICAEN, ENSICAEN, CNRS, GREYC, 14000 Caen, France
e-mail: kevin.gosse@etudiant.univ-reims.fr, stephanie.jehan@ensicaen.fr
[2] XLIM Laboratory, UMR CNRS 7252, University of Poitiers
e-mail: francois.lecellier@univ-poitiers.fr
[3] LITIS EA 4108 - QuantIF, University of Rouen
e-mail: su.ruan@univ-rouen.fr

***Abstract*— In this paper, we propose to compare different methods for tumor segmentation in positron emission tomography (PET) images. We first propose to tackle this problem under the umbrella of shape optimization and 3D deformable models. Indeed, 2D active contours have been widely investigated in the literature but these techniques do not take advantage of 3D informations. On the one hand, we use the well-known model of Chan and Vese. On the other hand we use a criterion based on parametric probabilities which allows us to test the assumption of Poisson distribution of the intensity in such images. Both will be compared to their 2D equivalent and to an improved random-walker algorithm. For this comparison, we use a set of simulated, phantom and real sequences with a known ground-truth and compute the corresponding Dice Coefficients. We also give some examples of 2D and 3D segmentation results.**

***Keywords*— Biomedical imaging, Active contours, Deformable models, level sets, PET imaging, Random walk, Poisson law, segmentation.**

I. INTRODUCTION

The current work is devoted to the segmentation of tumors regions in Positron Emission Tomography (PET) images. Indeed such medical images are powerful for cancer tumors visualization by detecting photons from a radiotracer localized in abnormals cells. However the conception of automatic segmentation methods in these images is difficult due to different factors and notably a high level of noise, a low contrast and unclear boundaries. The patient breathing can lead to motion artifacts and noise and there is also a large variability in shape or even in texture for the tumors to be segmented. A wide variety of image segmentation techniques have been proposed up to now and a large review of these numerous methods used to segment PET images is available in [1].

In this paper, due to the shape variability of tumors, we rather decide to give a new insight on region-based deformable models (active contours or surfaces) for the segmentation of tumors in PET images. Active contours have been introduced by Kass, Witkin and Terzopoulos [2] and later by Caselles et al [3] and were originally boundary methods. Due to the low contrast and unclear boundaries of PET images, we focus on region-based models where region functionals are used in addition to boundary functionals. Such powerful methods have appeared later. Introduced by [4] and [5], they have been further developed in [6], [7], [8]. In [9], [10], [11], [12], [13], the authors propose to take advantage of the minimization of statistical functionals that involve parametric pdfs of the exponential family in order to better modelize the distribution of the intensity in the regions to segment. In PET images, the distribution can be assimilated to a Poisson law because it is based on the detection of Photons in the tumoral zone. In order to verify this assumption, we propose to compute the evolution equation of a deformable model that will minimize the anti-log-likelihood function of a Poisson distribution. We compare it to the classical Chan and Vese method [7] which appears to be usually very robust for segmentation. We also propose to take benefit of a 3D segmentation model based on the level set method [14]. We compare the 3D segmentation to the result obtained using 2D segmentations of each slice. Moreover, we also compare these methods to two random-walker models, the classical one from [15] and the Locally Adaptive Random Walk (LARW) from [16]. The comparison of all these methods is performed on the basis of a strong database that includes simulated images, real phantom acquisitions and clinical data. The ground truth delineations provided with this database allow us to compute the Dice Coefficient as well as sensitivity and specificity parameters in order to objectively compare the different assumptions, implementations or methods.

This paper is organized as follows: we briefly remind the principle of region-based deformable models and we explain both Chan and Vese and Poisson model in Section 2. The random-walker model used as a comparison with active contours is presented in Section 3. Experimental results are discussed in Section 4. We finally conclude and give some perspectives.

II. ACTIVE CONTOURS

Let $\mathcal{U}$ be a class of domains (open, regular bounded sets, i.e. C^2) of $\mathbb{R}^n$ ($n = 2$ or 3), and Ω_i an element of $\mathcal{U}$ of boundary $\partial\Omega_i$. The image domain is denoted by Ω_I. A region-based segmentation problem aims at finding a partition of Ω_I in 2 regions $\{\Omega_{in}, \Omega_{out}\}$ that minimizes the following criterion:

$$E(\Omega_{in}, \Omega_{out}, \Gamma) = J_r(\Omega_{in}) + J_r(\Omega_{out}) + \alpha J_{reg}(\Gamma), \quad (1)$$

where $J_r(\Omega_i)$ describes the homogeneity of the region Ω_i and will be further developed in sections A and B according to the underlying distribution model. The term Γ denotes the common interface between the two regions. The energy term J_{reg} is a regularization term, balanced with a positive real parameter α, which is chosen as $J_{reg} = \int_\Gamma da$ where da represents an area element. In 2D, this term corresponds to the minimization of the curve length and in 3D to the minimization of the surface area. This term will help us to provide a smooth curve or surface to delineate the tumor.

In order to minimize such a criterion, we propose to classically perform a shape gradient descent by computing the evolution equation of an active contour using shape derivation tools. The interested reader may refer to [17] [18] [19] for further details in shape derivation methods and active contours based on shape gradients. Formally, from the computed shape derivatives, we can deduce the evolution equation that will drive the active contour towards a minimum of the criterion in the following general form:

$$\frac{\partial\Gamma(p,\tau)}{\partial\tau} = v(x,\Omega)N(x) \quad (2)$$

with $v(x,\Omega)$ the velocity of the active contour (in 2D) or surface (in 3D) deduced from the shape derivatives. The velocity is directed along the unit inward normal N of $\partial\Omega$. The active contour evolves from an initial curve $\Gamma(\tau = 0) = \Gamma_0$. In the equation (2), we have $x = \Gamma(p,\tau)$.

Let us now detail the two main criteria that we have tested for PET segmentation and the corresponding evolution equations.

A. THE CHAN-VESE MODEL

When looking for an homogeneous region, a classic and robust model was proposed in [7] by Chan and Vese, originally inspired by the Mumford-Shah functional [20]. This criterion implies the use of the mean value of the intensity inside the region Ω_i, denoted by μ_i. We then search for the partition of the image which minimizes the square error between the intensity and the mean value of the region inside each region by using the following region descriptor J_r in criterion (1):

$$J_r(\Omega_i) = \int_{\Omega_i} (I(\mathbf{x}) - \mu_i(\Omega_i))^2 d\mathbf{x} \quad \text{with} \quad i = in \,\text{or}\, out \quad (3)$$

The shape derivative of this criterion can be found in [18] [19] and leads to the following velocity term in equation (2):

$$v(x,\Omega_{in},\Omega_{out}) = (I-\mu_{in})^2 - (I-\mu_{out})^2 + \alpha\kappa, \quad (4)$$

where κ is the curvature of Γ. This model is implicitely based on the assumption of a Gaussian model with a fixed variance and a piece-wise constant image model.

B. THE POISSON MODEL

Besides the well-known model of Chan and Vese, we propose to investigate a model based on a Poisson law. Indeed, our assumption lies on the Poisson nature of photon-counting in PET images as first investigated by [21] for segmentation. We focus here on the minimization of the anti-log likelihood classically used by [6], [22] and [11], [12]. In that case, the region based term is the following :

$$J_r(\Omega_i) = -\int_{\Omega_i} \log p(I(x),\lambda_i) dx, \quad (5)$$

with p the Poisson distribution of the intensity I inside the region Ω_i indexed with the parameter λ_i ($i = in$ or out), such that:

$$p(I(x),\lambda_i) = \frac{\lambda_i^{I(x)} e^{-\lambda_i}}{I(x)!}.$$

We can calculate the maximum likelihood estimate of the parameter λ_i as follows:

$$\widehat{\lambda}_{i\,MV} = \frac{1}{|\Omega_i|}\int_{\Omega_i} I(x)dx. \quad (6)$$

The log-likelihood is then:

$$\log\left(p(I(x),\widehat{\lambda}_{i\,MV}\right) = I(x)\log\left(\widehat{\lambda}_{i\,MV}\right) - \widehat{\lambda}_{i\,MV} - \log(I(x)!),$$

which leads to the following region-based term:

$$\begin{aligned} J_r(\Omega_i) = \widehat{\lambda}_{i\,MV}|\Omega_i| + \int_{\Omega_i}\log(I(x)!)dx \\ - \log\left(\widehat{\lambda}_{i\,MV}\right)\int_{\Omega_i} I(x)dx. \end{aligned} \quad (7)$$

We then propose to compute the shape derivative of the previous region-based term which leads to the following theorem:

Theorem 1: The shape derivative in the direction V of the functional (5), with p the pdf of Poisson distribution and $\widehat{\lambda}_{i\,MV}$ the parameter of this distribution estimated by the maximum likelihood estimate, is

$$< J_r'(\Omega), V >= -\int_{\partial\Omega} v_i(\mathbf{x},\Omega) < V, N > da$$

where $v_i(\mathbf{x},\Omega) = \left(-I(\mathbf{x})\log(\widehat{\lambda}_{i\,MV}) + \widehat{\lambda}_{i\,MV} + \log(I(x)!)\right)$.

The complete proof is given in Appendix. Note that a more general proof for shape derivatives of statistical region-based terms using pdfs of the exponential family can be found in [12]. The proof for the Poisson law is here given for completeness.

Using the fact that the two regions Ω_{in} and Ω_{out} share the same interface with opposite normals, we can get our velocity term $v(x,\Omega_{in},\Omega_{out})$ for equation (2) :

$$\begin{aligned} v(x,\Omega_{in},\Omega_{out}) = &- I\,\log(\widehat{\lambda}_{in_{MV}}) + \widehat{\lambda}_{in_{MV}} \\ &+ I\,\log(\widehat{\lambda}_{out_{MV}}) - \widehat{\lambda}_{out_{MV}} + \alpha\kappa. \end{aligned} \quad (8)$$

C. IMPLEMENTATION OF THE ACTIVE CONTOUR

As far as the numerical implementation is concerned, we use the level set method introduced in [14]. The key idea is to introduce an auxiliary function $U(x,\tau)$ such that $\Gamma(\tau)$ is the zero level set of U. The function U is often chosen to be the signed distance function of $\Gamma(\tau)$. The evolution equation then becomes:

$$\frac{\partial U(\mathbf{x},\tau)}{\partial \tau} = v(\mathbf{x},\Omega_{in},\Omega_{out})|\nabla U(\mathbf{x},\tau)|. \tag{9}$$

This method is accurate and allows to automatically handle the topological changes of the initial curve. It can be used in 2D and 3D. For the 3D implementation, κ is chosen as the mean curvature. The 3D implementation is interesting in the case of PET sequences since it allows to introduce automatically a global 3D regularization term. In the experimental results, we show that the 3D segmentation allows a better segmentation of tumors than the 2D segmentation applied to each slice separately.

III. THE RANDOM-WALKER MODEL

In this section, we first explain the classical random walk algorithm [15] and then its extension for PET segmentation known as the LARW (Locally Adaptive Random Walk) method [16].

A. CLASSICAL RANDOM WALK (RW)

In this model, an image is considered like a graph $G = (V,E)$. Each voxel is associated with a node of the graph and edges link adjacent voxels. This method requires a small number, called seeds, of labeled voxels as an initial step. The key idea behind this method is to imagine a random walker starting from each unlabeled voxels. This random-walker has a certain probability to first arrive at a specific seed. The label is then chosen as the same label as the seed with the maximum probability of arrival of the random-walker. A common weight used for edges is:

$$\omega_{ij} = \exp\left[-\beta(g_i - g_j)^2\right], \tag{10}$$

where both g_i and g_j are the image intensity values at points i and j. The term β denotes a free parameter depending on the application.

We define the Laplacian matrix of the graph by

$$L_{ij} = \begin{cases} d_i & \text{if } i = j, \\ -\omega_{ij} & \text{if } v_i \text{ et } v_j \text{ are adjacent nodes,} \\ 0 & \text{otherwise.} \end{cases}$$

with $d_i = \sum \omega_{ij}$ for each node.

This matrix can be rearranged with labeled and unlabeled voxels as follows:

$$L = \begin{pmatrix} L_M & B \\ B^T & L_U \end{pmatrix},$$

where M and U correspond to labeled and unlabeled pixels. It has been shown in [15] that the solution of the random-walk for a specific label minimizes the following energy:

$$D[x] = \frac{1}{2}x^T L x = \frac{1}{2}\sum_{e_{ij}\in E} \omega_{ij}(x_i - x_j)^2,$$

which leads to the linear system:

$$L_U X = -B^T M. \tag{11}$$

B. LOCALLY ADAPTIVE RANDOM WALK (LARW)

An improved version of the classical random-walker algorithm was proposed in [16]. The proposed segmentation method initializes automatically seeds in tumor voxels using Fuzzy-C Means (FCM), and then delineates the tumor volume using the improved RW. They made two major changes to the algorithm described above. First, they changed the weight of edges to take care of the spatial distance between voxels. Equation (10) is then modified to:

$$\omega_{ij} = \exp\left[\frac{-\beta(g_i - g_j)^2}{h_{ij}}\right] \tag{12}$$

where the h_{ij} term is the spatial distance between voxels i and j.

They also proposed to strengthen the grouping of voxels having similar intensity by adding the likelihood of probability to each class (tumor and non tumor). Supposing each class k having a Gaussian distribution, their observation likelihood function can be written as:

$$p_k(I,\mu_k,\sigma_k) = \frac{1}{\sigma_k\sqrt{2\pi}}\exp\left[\frac{-(I-\mu_k)^2}{2\sigma_k^2}\right] \tag{13}$$

where μ_k and σ_k are respectively the mean and the variance of the class k. The matrix B^T is then modified

$$B' = p_k.B^T$$

which leads to the new linear system to solve

$$L_U X = -B'M \tag{14}$$

the complete algorithm is detailed in [16].

IV. EXPERIMENTAL RESULTS

A. DATA SET AND METHOD OF EVALUATION

In order to test the different algorithms, we use the training data set provided by the MICCAI PETSEG Challenge [23]. Following recommendations by the TG2111 [24], this evaluation dataset consists of a mixture of numerical simulations with realistic uptake distributions and a variety of tumor shapes, physical phantoms acquisitions, and real clinical images [25], [26]. Simulated images consist of realistic tumors embedded within numerical phantoms, with corresponding SIMSET [27] or GATE [28], [29] simulated data to better account for the physics of PET acquisition. Voxel-by-voxel ground-truth is available from the simulations. The physical phantoms are zeolites with different sizes and shapes incorporated in an anthropomorphic phantom, with repeated acquisitions of the same zeolites [30]. The surrogate of truth for these images is the corresponding high resolution CT, thresholded as to obtain the exact known volume of the zeolite. Clinical images are lung [31], [32] and head and neck [33] tumors, with either histopathology-based contours [31], [33] or a consensus of several manual delineations by experts [32] obtained with STAPLE [34] to serve as a surrogate of truth.

Image sequences are then divided into three parts.

1) Sequences 1 to 6 : simulated images (GATE and SIMSET).
2) Sequences 7 to 15 : real phantom acquisitions
3) Sequences 16 to 19 : patient clinical data

The different images resolutions are detailed in Table 1.

Table 1. Resolutions of the different sequences of the PETSEG data set

Sequence	Name	Dimensions
1	Simu_2_TEP_4	27x35x23
2	Simu_2_TEP_1	15x15x15
3	Simu_2_TEP_2	17x18x15
4	Simu_2_TEP_3	17x23x18
5	Simu_1_PET2	32x26x34
6	Simu_1_PET1	32x26x34
7	phantom_1_PET2	22x17x17
8	phantom_1_PET3	22x17x17
9	phantom_1_PET1	22x17x17
10	phantom_2_PET3	13x14x12
11	phantom_2_PET1	13x14x12
12	phantom_2_PET2	13x14x12
13	phantom_3_PET3	21x21x13
14	phantom_3_PET2	21x21x13
15	phantom_3_PET1	21x21x13
16	clinical_3_PET	28x23x28
17	clinical_2_4mm_PET	13x14x14
18	clinical_2_2mm_PET	25x25x23
19	clinical_1_PET	19x18x15

The different segmentation results from the above algorithms were compared to the provided ground-truth using the Dice Similarity Coefficient which measures the extent of spatial overlap between two binary sequences X and Y and is expressed as follows:

$$\mathrm{DC} = \frac{2|X \cap Y|}{|X| + |Y|} \tag{15}$$

where $|X|$ stands for the area of X.

We also use the sensitivity and the specificity coefficients. Sensitivity, also called the true positive rate (TPR), is the proportion of the tumor correctly identified by the algorithm:

$$\text{Sensitivity} = \frac{\text{Number of true positives}}{\text{Size of the tumor}} \tag{16}$$

Specificity, also called the true negative rate (TNR), is the proportion of non-tumor correctly identified as such:

$$\text{Specificity} = \frac{\text{Number of true negatives}}{\text{Size of the non-tumor}} \tag{17}$$

B. 2D AND 3D COMPARISON

For this experiment, we perform 2D and 3D segmentations using the level set approach detailed in section II with both the Chan-Vese and the Poisson models. Then, we compute the Dice Similarity Coefficient for each slice of each sequence which allows us to compare 2D and 3D segmentations for a same model. In Fig. 1, we trace the obtained DC values for each segmented slice of the first sequence using the Chan-Vese model. The tumor is located between the slices 5 to 20 which corresponds to the numbers 1 to 16 in the Fig.1 .

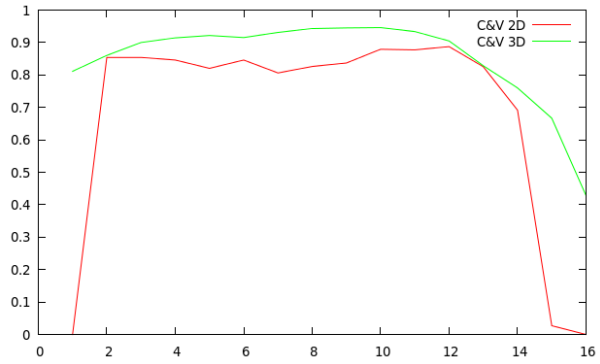

Fig. 1. 2D and 3D segmentation comparison on a simulated image sequence (sequence 1). The graph represents the values of the DC coefficient computed for each 2D slice (from 1 to 16) between the expert contour and the resulting contour of the 2D segmentation method (in blue) and the 3D one (in red).

Experimental results, not reported here for space reasons, are very similar for other sequences and Poisson model. It clearly appears that considering the whole 3D information improves segmentation results especially at the beginning and the end of the 3D sequences when tumors tend to be less visible and very small.

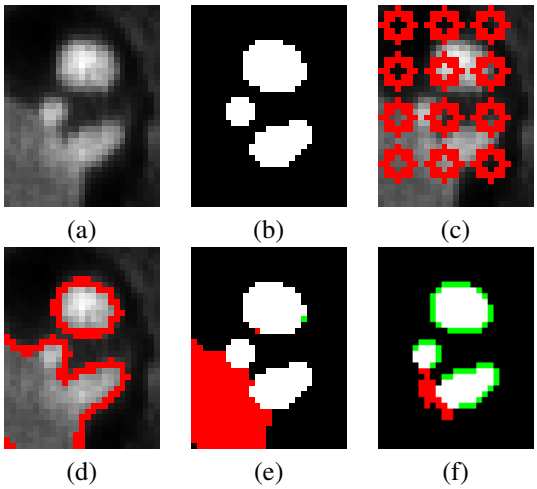

Fig. 2. a. PET image, b. Ground-Truth, c. Initial contour, d. Final contour in red for 2D Chan-Vese segmentation (smoothing coefficient $\alpha = 1$), e. 2D segmentation comparison with ground-truth (false positive in red and false negative in green), f. 3D segmentation comparison with ground-truth (smoothing coefficient $\alpha = 1$, false positive in red and false negative in green).

In the example given in Fig.2, we can see that the 2D segmentation shows a lot of false positives. Indeed, it takes into account the lower left of the image which is of similar intensity, but not part of the tumor. The effect is clearly less visible in 3D.

C. METHODS COMPARISON

For this second experiment, we propose to compare the different methods presented in this paper. We limit ourselves with 3D segmentation since we have seen in the previous

section that 3D segmentation outperforms 2D segmentation in all cases. For the random-walker method, we make two versions of the algorithm. The first one is the classical random-walker algorithm [15] described briefly in section III. The second one is the Locally Adaptive Random-Walk version from [16] with minor changes (auto-initialization of seed's background like the one's from the tumor and unsystematic median-filtering).

First of all, in Fig.3 and Fig. 4, we give two examples of the different segmentation results and corresponding contours obtained on two extracted slices (one from the simulated set and one from the clinical set). For each method, we compare the mask to the ground truth (expert segmentation) and we show in red the false positive points and in green the false negative points. We can observe that both methods are able to segment accurately the tumor from the simulated set (Fig. 3). In the case of more complicated clinical data with non homogeneous tumors (see Fig. 4), the different automatic methods are less accurate. In this case the Poisson model leads to less false negative but more false positive than the Chan and Vese methods. For such images, a pre-processing such as denoising or contrast enhancement could be valuable.

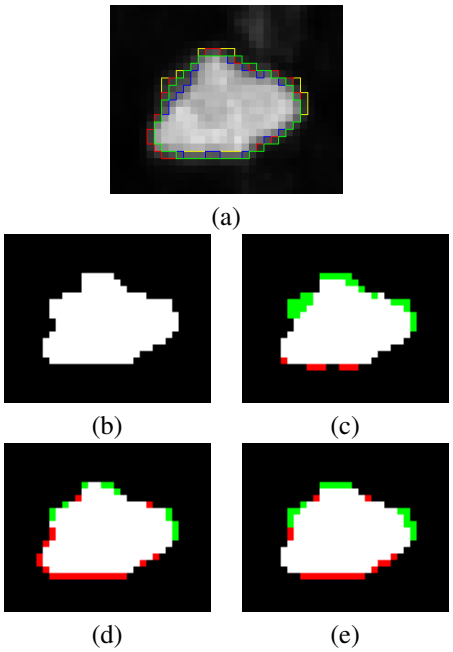

Fig. 3. a. PET image from the simulated set with the different contours (in yellow the ground truth, in blue the 3D Chan and Vese segmentation, in red the 3D Poisson segmentation and in green the LARW segmentation). We also display the masks of the ground truth in b., of the Chan and Vese segmentation in c., of the Poisson segmentation in d. and of the LARW segmentation in e. For the different methods, the false positives are shown in red and the false negative in green.

Let us now consider the computation of the DC (Dice Coefficient) between the different methods and the ground truth for all the sequences of the training data-set (Table 2).

Considering these results it appears that the assumption of

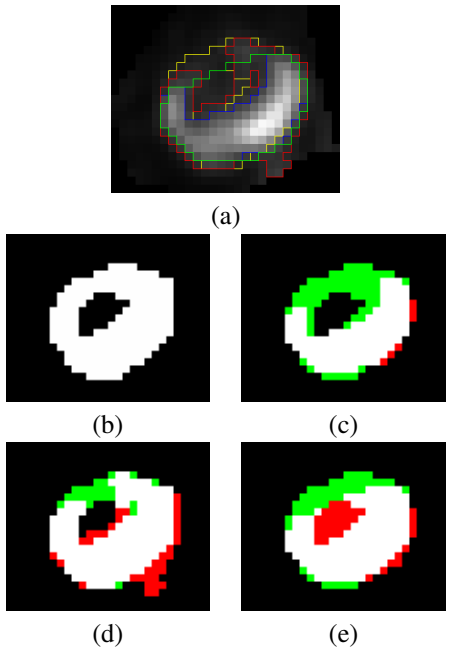

Fig. 4. a. PET image from the clinical set with the different contours (in yellow the ground truth, in blue the 3D Chan and Vese segmentation, in red the 3D Poisson segmentation and in green the LARW segmentation). We also display the masks of the ground truth in b., of the Chan and Vese segmentation in c., of the Poisson segmentation in d. and of the LARW segmentation in e. For the different methods, the false positives are shown in red and the false negative in green.

Poisson distribution in PET images is relatively true especially for simulated images (sequences 1 to 6). In the case of real phantom acquisitions (sequences 7 to 15), the method is less robust than the Chan and Vese method. Indeed the piece-wise constant model assumed by the Chan-Vese method seems more robust in this case due to the fact that the phantom has a constant intensity. As far as clinical data are concerned, the Chan-Vese model and Poisson model seem quite equivalent. The Chan and Vese method is less accurate in some cases (sequences 16 and 18) due to the low contrast and more accurate in sequences 17 and 19. In fact the real distribution model of the intensity in these images is probably a mixture between a Poisson law and a Gaussian model due to the reconstruction process and also to the artifacts encountered in acquisition methods (patient breathing, low resolution, camera noise model). Globally, for all the different sequences, the Chan and Vese method is more robust.

When computing the specificity and sensitivity coefficients (see Table 3), we can observe that the Poisson method offers very good sensitivity coefficients but lowest specificity values. On the contrary, the LARW method shows very good specificity values with lower sensitivity values. The Chan and Vese method offers a good compromise between sensitivity and specificity coefficients.

The 3D Chan-Vese and LARW methods are the most robust algorithms and can perform great segmentation in many kind

Table 2. Comparison of Dice coefficients of the different methods.

Sequence	Chan-Vese 3D	Poisson 3D	RW	LARW
1	0.9040	0.8489	0.7783	0.8679
2	0.9448	0.9441	0.9061	0.8764
3	0.8674	0.8766	0.7813	0.8121
4	0.8974	0.9764	0.8357	0.8017
5	0.8789	0.8970	0.7491	0.8702
6	0.9012	0.8924	0.7283	0.8747
7	0.8221	0.7791	0.8070	0.7747
8	0.8082	0.7824	0.8030	0.7445
9	0.8025	0.7864	0.8057	0.7461
10	0.7600	0.5112	0.8105	0.7972
11	0.7614	0.4908	0.7122	0.8133
12	0.7415	0.5229	0.7513	0.7778
13	0.8235	0.5100	0.8192	0.8435
14	0.7958	0.4946	0.8029	0.8584
15	0.8014	0.5122	0.8346	0.8509
16	0.8492	0.8792	0.8516	0.8469
17	0.7630	0.7323	0.7301	0.6742
18	0.7629	0.7688	0.6907	0.7171
19	0.6444	0.5714	0.5570	0.6743
Mean	0.8158	0.7251	0.7766	0.8014

Table 3. Comparison of Sensitivity (TPR) and Specificity (TNR) parameters.

	Chan-Vese 3D		Poisson 3D		LARW	
Sequence	TPR	TNR	TPR	TNR	TPR	TNR
1	0.8431	0.9927	0.9770	0.8929	0.7967	0.9870
2	0.9032	0.9990	0.9912	0.9878	0.7801	1
3	0.8607	0.9770	0.9694	0.9551	0.8036	0.9675
4	0.8139	1	0.9581	0.9992	0.6696	0.9998
5	0.8053	0.9965	0.9268	0.9823	0.8609	0.9851
6	0.8750	0.9915	0.9670	0.9746	0.8901	0.9816
7	0.7428	0.9930	0.9357	0.9494	0.6608	0.9951
8	0.7283	0.9920	0.9164	0.9538	0.6254	0.9941
9	0.7154	0.9927	0.9084	0.9564	0.6190	0.9956
10	0.95	0.9791	1	0.9273	0.7125	0.9971
11	0.9375	0.98	1	0.9211	0.7625	0.9957
12	0.95	0.9767	1	0.9306	0.7	0.9962
13	0.9739	0.9920	1	0.9607	0.8435	0.9968
14	0.9826	0.99	1	0.9582	0.8435	0.9975
15	0.9826	0.9904	1	0.9610	0.8435	0.972
16	0.7551	0.9949	0.9625	0.9490	0.8071	0.9778
17	0.7523	0.9799	0.8692	0.9537	0.5607	0.9906
18	0.7178	0.9765	0.8442	0.9495	0.6596	0.9741
19	0.7973	0.9466	0.8640	0.9085	0.7867	0.9569
Mean	0.9460	0.9863	0.9521	0.9511	0.7487	0.9874

of images. We can observe that Chan-Vese method tends to sub-segment tumors and it is worth noting that Chan-Vese segmentation is often a subset of Poisson segmentation. An interesting fact for RW and LARW is the importance of the initialization of seeds. The more the better is not necessary true here. If we have more information on where the background is exactly, and made no change in tumor's seeds, it will necessarily sub-segment the previous segmentation because non-labeled voxels have more probability to reach background then. In a general way, we have to choose correctly the amount of seeds for background and tumor. Here, we choose them in order to obtain the best results. More detailed experimental results can be found in [16].

V. CONCLUSION AND PERSPECTIVES

In this paper, we propose to investigate the use of 2D and 3D deformable models for PET images segmentation. These deformable models are currently based on the minimization of statistical criteria and are implemented using the level set method. In one of the tested criterion, we take into account the Poisson distribution of PET images. Our results show a great improvement of the segmentation from 2D to 3D and validate the implication of Poisson law in PET images. However, the Chan-Vese model (implicitely based on the assumption of a Gaussian model) still remains the most robust algorithm and gives comparable results to the LARW method [16]. Our ongoing research is now directed towards two main challenges. First of all, the use of an improved statistical model based on a mixture of a Poisson and a Gaussian law could be valuable. Secondly, an intelligent fusion of the different segmentation results may also be investigated in order to improve the segmentation results.

VI. ACKNOWLEDGEMENT

We would like to thank the organizing committee of the MICCAI PETSEG Challenge [23] for their permission to publish our evaluation results using their training database.

APPENDIX
PROOF OF THEOREM 1

In the case of Poisson distribution, the region-based term that we want to derive according to the domain Ω is the following:

$$\begin{aligned} J_r(\Omega) &= -\int_\Omega \log p(I(x),\lambda)dx \\ &= \widehat{\lambda}_{MV}|\Omega| + \int_\Omega \log(I(x)!)dx - \log\left(\widehat{\lambda}_{MV}\right)\int_\Omega I(x)dx \end{aligned}$$

We have to compute the shape derivative of $J_r(\Omega)$. For this purpose, we remind here the following fundamental theorem which establishes a relation between the shape derivative of region-based terms of the form $J_r(\Omega) = \int_\Omega k(x,\Omega)dx$:

Theorem 2: The shape derivative $< J_r'(\Omega), V >$ of the functional $J_r(\Omega) = \int_\Omega k(x,\Omega)dx$ in the direction V is

$$< J_r'(\Omega), V >= \int_\Omega k'(x,\Omega,V)dx - \int_{\partial\Omega} k(x,\Omega) < V \cdot N > da$$

where k' is the shape derivative of k. The term N denotes the unit inward normal to $\partial\Omega$ and da its area element (in $\mathbb{R}^2$, we have $da = ds$ where s stands for the arc length).

Using this theorem and the equation of the Maximum Likelihood estimate for the Poisson parameter λ given in (6), we find:

$$\begin{aligned} <J_r'(\Omega), V > &= -\int_{\partial\Omega} \log(I(x)!) < V \cdot N > da \\ &\quad + |\Omega| < \widehat{\lambda}_{MV}, V > -\widehat{\lambda}_{MV}\int_{\partial\Omega} < V \cdot N > da \\ &\quad - \frac{< \widehat{\lambda}_{MV}, V >}{\widehat{\lambda}_{MV}}\int_\Omega I(x)dx + \log\left(\widehat{\lambda}_{MV}\right)\int_{\partial\Omega} I(x)da \\ &= \int_{\partial\Omega}\left(\log\left(p\left(I(x),\widehat{\lambda}_{MV}\right)\right)\right) < V, N > da \\ &\quad + < \widehat{\lambda'}_{MV}, V > |\Omega|\left(1 - \frac{\overline{I}}{|\Omega|\,\widehat{\lambda}_{MV}}\right) \end{aligned}$$

where $\overline{I} = \int_\Omega I(x)dx$ and $< \widehat{\lambda'}_{MV}, V >= -\frac{1}{|\Omega|}\int_{\partial\Omega}(I(\mathbf{x}) - \widehat{\lambda_{MV}}) < V \cdot N > da$.
Since $\left(1 - \frac{\overline{I}}{|\Omega|\,\widehat{\lambda}_{MV}}\right) = 0$, we can then conclude that :

$$< J_r'(\Omega), V >= \int_{\partial\Omega} \log\left(p(I(x), \widehat{\lambda}_{MV})\right) < V \cdot N > da$$

where $p(I(x), \widehat{\lambda}_{MV})$ is the Poisson pdf model.

REFERENCES

[1] B. Foster, U. Bagci, A. Mansoor, Z. Xu, and D. J. Mollura, "A review on segmentation of positron emission tomography images," *Computers in Biology and Medicine*, vol. 50, pp. 76–96, 2014.

[2] M. Kass, A. Witkin, and D. Terzopoulos, "Snakes: Active contour models," *Int. J. of Computer Vision*, vol. 1, pp. 321–332, 1988.

[3] V. Caselles, R. Kimmel, and G. Sapiro, "Geodesic active contours," *Int. J. of Computer Vision*, vol. 22, no. 1, pp. 61–79, 1997.

[4] L. Cohen, E. Bardinet, and N. Ayache, "Surface reconstruction using active contour models," in *SPIE Conference on Geometric Methods in Computer Vision*, San Diego, 1993.

[5] R. Ronfard, "Region-based strategies for active contour models," *Int. J. of Computer Vision*, vol. 13, pp. 229–251, 1994.

[6] S. C. Zhu and A. Yuille, "Region competition: Unifying snakes, region growing, and Bayes/MDL for multiband image segmentation," *IEEE Trans. Pattern Anal. and Mach. Intell.*, vol. 18, no. 9, pp. 884–900, Sept. 1996.

[7] T. F. Chan and L. A. Vese, "Active contours without edges," *IEEE Trans. on Image Processing*, vol. 10, no. 2, pp. 266–277, 2001.

[8] N. Paragios and R. Deriche, "Geodesic active regions: A new paradigm to deal with frame partition problems in computer vision," *J. of Visual Communication and Image Representation*, vol. 13, pp. 249–268, 2002.

[9] P. Martin, P. Réfrégier, F. Goudail, and F. Guérault, "Influence of the noise model on level set active contour segmentation," *IEEE Trans. on Pattern Analysis and Machine Intelligence*, vol. 26, pp. 799–803, 2004.

[10] F. Galland, N. Bertaux, and P. Réfrégier, "Multi-component image segmentation in homogeneous regions based on description length minimization: Application to speckle, Poisson and Bernoulli noise," *Pattern Recognition*, vol. 38, pp. 1926–1936, 2005.

[11] F. Lecellier, S. Jehan-Besson, J. Fadili, G. Aubert, and M. Revenu, "Statistical region-based active contours with exponential family observations," in *ICASSP*, 2006, vol. 2, pp. 113–116.

[12] F. Lecellier, J. M. Fadili, S. Jehan-Besson, G. Aubert, and M. Revenu, "Region-based active contours with exponential family observations," *J. of Mathematical Imaging and Vision*, vol. 36, no. 1, pp. 28–45, 2010.

[13] S. Jehan-Besson, F. Lecellier, J. Fadili, G. Nee, and G. Aubert, *Biomedical diagnostics and clinical technologies : Applying high performance cluster and Grid Computing*, chapter Medical image segmentation and tracking through the maximisation or the minimisation of divergences between pdfs, pp. 34–61, IGI global, 2011.

[14] S. Osher and J. A. Sethian, "Fronts propagating with curvature-dependent speed: Algorithms based on Hamilton-Jacobi formulations," *J. of Computational Physics*, vol. 79, no. 1, pp. 12–49, 1988.

[15] L. Grady, "Random walks for image segmentation," *IEEE Trans. Pattern Anal. and Mach. Intell.*, vol. 28, no. 11, pp. 1768–1783, 2006.

[16] D.P. Onoma, S. Ruan, S. Thureau, L. Nkhali, R. Modzelewski, G.A. Monnehan, P. Vera, and I. Gardin, "Segmentation of heterogeneous or small FDG PET positive tissue based on a 3D-locally adaptive random walk algorithm," *Computerized Medical Imaging and Graphics*, vol. 38, no. 8, pp. 753–763, 2014.

[17] M. C. Delfour and J. P. Zolésio, *Shapes and Geometries*, SIAM Advances in Design and Control, 2011.

[18] S. Jehan-Besson, M. Barlaud, and G. Aubert, "DREAM^{2}S: Deformable regions driven by an Eulerian accurate minimization method for image and video segmentation," *Int. J. of Computer Vision*, vol. 53, no. 1, pp. 45–70, 2003.

[19] G. Aubert, M. Barlaud, O Faugeras, and S. Jehan-Besson, "Image segmentation using active contours : Calculus of variations or shape gradients," *SIAM Applied Mathematics*, vol. 63, pp. 2128–2154, 2003.

[20] D. Mumford and J. Shah, "Optimal approximations by piecewise smooth functions and associated variational problems," *Communications on Pure and Applied Mathematics*, vol. XLII, no. 5, pp. 577–685, 1989.

[21] T. F. Chan, H. Li, M. Lysaker, and X.-C. Tai, "Level set method for positron emission tomography," *Int. J. of Biomedical Imaging*, p. 15 pages, 2007.

[22] F. Goudail and P. Réfrégier, *Statistical image processing techniques for noisy images*, Plenum publishers, 2004.

[23] France Life Imaging Information Analysis and Management, "PET segmentation challenge using a data management and processing infrastructure," https://portal.fli-iam.irisa.fr/petseg-challenge/overview, 2016.

[24] M. Hatt, J. A. Lee, C. R. Schmidt, I. El Naqa, C. Caldwell, E. De Bernardi, W. Lu, S. Das, X. Geets, V. Gregoire, R. Jeraj, M. MacManus, O. Mawlawi, U. Nestle, A. Pugachev, H. Schoder, T. Schepherd, E. Spezi, D. Visvikis, H. Zaidi, and A. Kirov, "Classification and evaluation strategies of auto-segmentation approaches for PET report of the american association of physicists in medicine task group 211," Tech. Rep., The American Association of Physicists in Medicine Task group 211, 2016, Medical Physics, proof under revision.

[25] T. Shepherd, B. Berthon, P. Galavis, E. Spezi, A. Apte, J. Lee, D. Visvikis, M. Hatt, E. de Bernardi, S. Das, I. El Naqa, U. Nestle, C. Schmidtlein, H. Zaidi, and A. Kirov, "Design of a benchmark platform for evaluating PET-based contouring accuracy in oncology applications," *Eur. J. Nucl. Med. Mol. Imag.*, vol. 39, pp. S264–S264, 2012.

[26] B. Berthon, E. Spezi, P. Galavis, T. Shepherd, A. Apte, M. Hatt, H. Fayad, E. De Bernardi, C. Soffientini, C. R. Schmidtlein, I. El Naqa, R. Jeraj, W. Lu, S. Das, H. Zaidi, O. Mawlawi, D. Visvikis, J. A. Lee, and A. Kirov, "Towards a standard for the evaluation of PET auto-segmentation methods: requirements and implementation," *Med. Phys.*, proof under submission 2016.

[27] M. Aristophanous, B. C. Penney, and C. A. Pelizzari, "The development and testing of a digital PET phantom for the evaluation of tumor volume segmentation techniques," *Med. Phys.*, vol. 35, no. 7, pp. 3331–42, 2008.

[28] A. Lemaitre, P. Segars, S. Marache, A. Reilhac, M. Hatt, S. Tomei, C. Lartizien, and D. Visvikis, "Incorporating patient specific variability in the simulation of realistic whole body 18F-FDG distributions for oncology applications," *Proceedings of the IEEE*, vol. 9, no. 12, 2009.

[29] P. Papadimitroulas, G. Loudos, A. Le Maitre, M. Hatt, F. Tixier, N. Efthimiou, G. C. Nikiforidis, D. Visvikis, and G. C. Kagadis, "Investigation of realistic PET simulations incorporating tumor patient's specificity using anthropomorphic models: creation of an oncology database," *Med. Phys.*, vol. 40, no. 11, pp. 112506, nov. 2013.

[30] F. Zito, E. De Bernardi, C. Soffientini, C. Canzi, R. Casati, P. Gerundini, and G. Baselli, "The use of zeolites to generate PET phantoms for the validation of quantification strategies in oncology," *Med. Phys.*, vol. 39, no. 9, pp. 5353–5361, sep. 2012.

[31] M. Wanet, J. A. Lee, B. Weynand, M. De Bast, A. Poncelet, V. Lacroix, E. Coche, V. Gregoire, and X. Geets, "Gradient-based delineation of the primary GTV on FDG-PET in non-small cell lung cancer: a comparison with threshold-based approaches, ct and surgical specimens," *Radiother. Oncol.*, vol. 98, no. 1, pp. 117–25, 2011.

[32] J. Lapuyade-Lahorgue, D. Visvikis, O. Pradier, C. Cheze Le Rest, and M. Hatt, "Speqtacle: An automated generalized fuzzy C-means algorithm for tumor delineation in PET," *Med. Phys.*, vol. 42, no. 10, pp. 5720, 2015.

[33] X. Geets, J. A. Lee, A. Bol, M. Lonneux, and V. Gregoire, "A gradient-based method for segmenting FDG-PET images: methodology and validation," *Eur J Nucl Med Mol Imag.*, vol. 34, no. 9, pp. 1427–38, 2007.

[34] S. K. Warfield, K. H. Zou, and W. M. Wells, "Simultaneous truth and performance level estimation (STAPLE): an algorithm for the validation of image segmentation," *IEEE Trans. on Medical Imaging*, vol. 23, no. 7, pp. 903–21, 2004.